

# Numerical simulation of short laser pulse relativistic self-focusing in underdense plasma

Piero Chessa<sup>a)</sup> and Patrick Mora

*Centre de Physique Théorique, Ecole Polytechnique, 91128 Palaiseau Cedex, France*

Thomas M. Antonsen, Jr.

*Institute for Plasma Research and Departments of Electrical Engineering and Physics, University of Maryland, College Park, Maryland 20742*

(Received 11 February 1998; accepted 4 June 1998)

Existing experimental results on relativistic self-focusing are interpreted by means of the particle code WAKE using the ponderomotive approximation to describe the laser-plasma interaction [P. Mora and T. M. Antonsen, Jr., *Phys. Plasmas* **4**, 217 (1997)]. Novel features of the code, such as gas medium ionization and an enhanced paraxial approximation, allow more confidence in data interpretation. Simulations where the pulse power is less or close to the critical value match the experimental data. The transmitted pulse spectrum is shown in this case to shift towards longer wavelengths. The pulse is shown to focus over the vacuum diffraction limit, while the energy is slowly depleted. Simulations of pulses above the critical power match experiment with reduced precision. This can be ascribed to beam filamentation. High energy depletion is expected in this case due to Raman instability. © 1998 American Institute of Physics. [S1070-664X(98)01809-6]

## I. INTRODUCTION

Relativistic laser-plasma interaction is one of the most interesting problems that the development of pulsed power laser technology permits us to investigate. With newly developed lasers, intensities up to  $10^{19}$  W/cm<sup>2</sup> can be reached, with a typical wavelength of 1  $\mu$ m.<sup>1</sup> The Lorentz factor of an oscillating electron in a laser pulse of intensity  $I$  and wavelength  $\lambda$  is given by

$$\gamma = \sqrt{1 + \frac{1}{2.74 \times 10^{18}} \left( \frac{\lambda}{\mu\text{m}} \right)^2 \frac{I}{\text{W/cm}^2}}.$$

Thus, relativistic effects are expected for the interaction of a super-intense laser pulse and the electrons of a plasma. These effects govern the collective response of electrons and result in a macroscopic effect on the laser pulse propagation.

The main relativistic signature in laser-plasma interaction is the lowering of natural plasma frequency,

$$\omega_{\text{rel}} = \sqrt{\frac{4\pi e^2 n_e}{\gamma m_e}},$$

where  $e$  is the elementary charge,  $n_e$  is the plasma electron density, and  $m_e$  is the rest mass of an electron. Since the optical properties of plasma depend on the ratio between  $\omega_{\text{rel}}$  and the laser frequency  $\omega_0$ , the laser pulse propagation is modified. The refractive index is given by

$$n = \sqrt{1 - \left( \frac{\omega_{\text{rel}}}{\omega_0} \right)^2}$$

and grows together with laser intensity  $I$ .

Two main phenomena can be explained by this refractive index change. The first is induced transparency, where a classically overdense plasma can have a real refractive index and become transparent to radiation, due to the relativistic decrease of plasma frequency.<sup>2,3</sup> Another important propagation phenomenon due to the modification of refractive index is relativistic self-focusing.<sup>4-8</sup> As a consequence of the radial variation of the electron quiver energy, due to the radial profile of laser pulse, the maximum refractive index is located on the optical axis. This distribution of index acts on the pulse as a positive lens. Roughly, one can say that a pulse undergoes a strong relativistic self-focusing when its power exceeds a critical value

$$P_{\text{cr}} = 16.2 \frac{n_c}{n_e} 10^9 \text{ W},$$

where  $n_c$  is the critical density associated with the laser frequency.<sup>4,5</sup> This critical power is defined as the power such that a plane phase pulse is equally focused and diffracted and propagates as in an optical guide.

Self-focusing experiments began a few years ago. In the first kind of experiment the scattering of part of the laser pulse by the plasma created in the interaction is measured.<sup>9-12</sup> In the first experiment of this kind, the dynamics of the laser pulse were diagnosed by wide angle imagery of the scattered-diffracted light. The resulting images were interpreted directly to represent the spatial distribution of the laser pulse.<sup>9</sup> A more recent experiment of this kind, based on 90° Thomson scattering,<sup>10</sup> has been analyzed by means of numerical models taking details of the scattering process into consideration.<sup>13,14</sup> As the scattered light intensity depends on both the incident laser pulse intensity and the electron density, a model of the electron density must be assumed. In developing a model to analyze these experiments some as-

<sup>a)</sup>Present address: Laboratoire d'Optique Appliquée, Ecole Polytechnique, 91128 Palaiseau Cedex, France.

sumptions were made. In particular, the electrons were assumed to respond adiabatically (that is, their inertia was neglected) and the laser pulse was assumed to evolve according to the paraxial approximation. This latter assumption requires the conservation of laser pulse energy. The refractive effects of gas ionization on the propagation of the pulse were neglected too. This approximation is based on the argument that the peak intensity of the laser pulse is very high compared to the threshold for hydrogen ionization. Nonetheless, recent experiments and simulations<sup>15</sup> show that plasma behavior may be strongly dependent on the ionization process, even at high peak intensities, and effects at the plasma boundary must be carefully tested.

More recently, experiments of a second kind have been performed.<sup>16,17</sup> These experiments use a transverse probe laser pulse in order to scan the plasma density just after the interaction pulse has passed. This technique allows, in principle, a more direct observation of the instantaneous refractive index distribution and indeed the results of these experiments are compatible with an interpretation in terms of relativistic self-focusing.

## II. SIMULATION CODE

This paper contains a series of simulations obtained with a recent version of the particle code WAKE,<sup>8</sup> where gas ionization is taken into account. The physical parameters have been chosen in order to match a recent experiment whose results have been published by Monot *et al.*<sup>10</sup> and by Chiron *et al.*<sup>14</sup>

The experimental results were obtained by the interaction of a 1.06  $\mu\text{m}$  wavelength laser pulse with a hydrogen jet. The pulse duration was about 400 fs. The transverse shape of the pulse was described by a Gaussian function, whose parameters have been set in order to match the peak intensity ( $I = 2.8 \times 10^{18} \text{ W/cm}^2$ ) and the waist radius ( $w_0 = 13 \mu\text{m}$ ) of the lowest order transverse mode of the beam as they have been measured by Chiron and co-workers.<sup>14</sup> The jet could be driven up to pressures of 0.32 bar of molecular hydrogen. It was flat-top over a propagation length of 2.5 mm and decreased to a residual vacuum pressure of  $10^{-4}$  bar with slopes of 0.5 mm.<sup>10</sup> According to the Thomson scattering plots by Monot and co-workers, the beam was focused at the beginning of the jet, 0.5 mm before its center.

Other numerical codes have already been used to interpret the experimental data by Monot *et al.* These calculations<sup>13,14</sup> explain some of the experimental observations, but, due to the fact that they use the adiabatic approximation for the electron response, they have left some questions about the importance of the transient effects and of the pulse shape modulation by Raman instability.<sup>7,18-20</sup> Apart from the consequences of the spectral spreading on the diffraction of the laser pulse, these models also neglect energy depletion arising from the pumping up of electron waves.<sup>8,20,21</sup> The gas medium ionization deserves some remarks too. It has been shown that in some cases the coupled actions of a finite transverse size of plasma and of transverse large excursions of electrons strongly affect the plasma response,<sup>15</sup> even if the peak intensity is far above the ioniza-

tion threshold. With the code WAKE it is possible to switch from a gas to a preformed homogeneous plasma medium and to test the effects of ionization on the propagation of the pulse.

The code WAKE is a two-dimensional (2D) particle code that can be used in cylindrical as well as in Cartesian geometry. Since the problem discussed in this paper has a cylindrical symmetry, all the results shown in the following have been obtained in this geometry.

The algorithm of the code is based upon three approximations: ponderomotive, quasistatic and extended paraxial. Electron trajectories are governed by the ponderomotive force of the laser field and the self-consistent electric and magnetic fields of the plasma wake. Within this approximation, their low frequency (i.e., plasma frequency band) components can be obtained by integration of the motion law

$$\frac{d}{dt} \bar{\mathbf{p}} = -e \left( \bar{\mathbf{E}} + \frac{\bar{\mathbf{v}}}{c} \wedge \bar{\mathbf{B}} \right) - \frac{e^2}{2\bar{\gamma}m_e c^2} \nabla |\bar{\mathbf{A}}|^2,$$

where the bar quantities are the low frequency band components,  $\mathbf{p}$  is the momentum,  $\mathbf{v}$  is the velocity,  $\mathbf{E}$  and  $\mathbf{B}$  are, respectively, the electric and magnetic fields and  $\tilde{\mathbf{A}}$  is the high frequency band component of the vector potential. The quasistatic approximation consists of assuming that the shape of the laser pulse and, consequently, that of the wake field, does not change significantly during the time of interaction with the longitudinally accelerated electrons. Electron motion is then defined by this equation together with the definition of the high frequency component of the momentum

$$\tilde{\mathbf{p}} = \frac{e}{c} \tilde{\mathbf{A}}$$

and of the averaged Lorentz factor

$$\bar{\gamma} = \sqrt{1 + \frac{|\bar{\mathbf{p}}|^2 + (e/c)^2 |\tilde{\mathbf{A}}|^2}{m^2 c^2}}.$$

The same approximation is used to work out ion trajectories. Due to the high masses, anyway, ions contribute less to the total current.

Pulse propagation is solved in an extended paraxial approximation, realized by introducing the variable  $\xi = ct - z$ , and by separating the laser vector potential into a complex amplitude modulating a plane wave

$$\tilde{\mathbf{A}}(r, \xi, z) = \hat{\mathbf{A}}(r, \xi, z) \exp(ik_0 \xi) + \text{c.c.},$$

where  $k_0$  is the central wave number of the laser pulse. The equation for the amplitude is obtained by dropping the smallest derivative in the wave equation. This gives the equation

$$\left( \nabla_{\perp}^2 + 2ik_0 \frac{\partial}{\partial z} - 2 \frac{\partial^2}{\partial \xi \partial z} \right) \hat{\mathbf{A}} = - \frac{\omega_p^2}{\gamma c^2} \hat{\mathbf{A}},$$

where  $\omega_p$  is the classical plasma frequency. The ratio  $\omega_p^2/\bar{\gamma}$  is obtained by averaging over an ensemble of particle trajectories. This equation governs the wave propagation following a spectral (i.e., frequency-by-frequency) paraxial ap-

proximation and is suitable for broad spectrum pulse propagation. These main features of the code have been presented in recent papers.<sup>8,22,23</sup>

Ionization of the gas medium is included in this version of the code. In the regime of pulse durations and intensities of interest, tunneling ionization<sup>24,25</sup> is dominant. This model is based on the semi-classical solution of the electron wave function evolution in a Coulomb field distorted by an external homogeneous and constant electric field. Ionization rates are given by this model for any atomic ion. The formula for the cycle averaged tunneling ionization rate in terms of the peak amplitude  $E$  of the wave electric field is

$$R_l(\eta) = \frac{\omega_{\text{at}}}{2} C_{n^*}^2 \frac{(2l+1)(l+|m|)!}{2^{|m|}|m|!(l-|m|)!} \times \frac{\epsilon_i}{\epsilon_H} (2\eta)^{2n^*-|m|-1} \exp\left(-\frac{2}{3}\eta\right),$$

where

$$\eta = \left(\frac{\epsilon_i}{\epsilon_H}\right)^{3/2} \frac{E_{\text{at}}}{E}$$

is the normalized electric field,  $\epsilon_i$  is the ionization potential,  $l$  and  $m$  are the initial angular momentum quantum numbers of the ion,  $n^*$  is the effective final main quantum number  $n^* = Z\sqrt{\epsilon_H/\epsilon_i}$ ,  $Z$  is the ionic charge after ionization and  $C_{n^*}^2 = [2\exp(1)/n^*]^{n^*}/\sqrt{2\pi n^*}$ . The constants  $\omega_{\text{at}}$  and  $E_{\text{at}}$ , being, respectively, the typical atomic frequency and field, are  $\omega_{\text{at}} = 4.16 \times 10^{16} \text{ s}^{-1}$  and  $E_{\text{at}} = 5.142 \times 10^9 \text{ V/cm}$ .

In the code, rates are used to compute the probabilities of ions emitting a number of electrons in an elementary time step. At a given position  $z$ , the time step being given by  $\Delta\xi/c$ , the probability for an ion to remain in the same ionization state is

$$P_0(\Delta\xi) = \exp[-R_1(E)\Delta\xi/c],$$

where  $R_1$  is the rate for the next ionization step and is a function of the local electric field  $E$ . The probability for the ion to emit a given number of electrons can be built by iteration taking  $P_0$  as a starting point and is

$$P_n(\Delta\xi) = \int_0^{\Delta\xi} P_{n-1}(\xi) \times \exp\left[-R_{n+1}(E)\frac{\Delta\xi-\xi}{c}\right] R_n(E)\frac{d\xi}{c}.$$

By recurrence one can show that the probability within an interval  $\Delta\xi$  for a decay with the emission of  $n$  electrons is given by the formula

$$P_n(\Delta\xi) = (-1)^n \prod_{h=1}^n R_h \sum_{j=1}^n \frac{\exp\left(-R_j\frac{\Delta\xi}{c}\right)}{\prod_{\substack{l=1 \\ l \neq j}}^{n+1} (R_j - R_l)},$$

where the  $k$ th ionization rate at the local value of the electric field has been indicated by  $R_k$ . Electrons are then emitted by a Monte Carlo procedure in agreement with these probabilities.

Because of the interaction with the electric field of the laser wave during the ionization process, electrons are, in principle, given an initial transverse low frequency drift according to a distribution. The average initial kinetic energy of the electrons has been shown by means of numerical three-dimensional (3D) quantum models of atoms in intense oscillating fields<sup>26</sup> to be of the order of the ionization potential. These energies, being very low compared with the quiver energies of the electrons during the interaction, can be neglected in our calculations. By the way, runs of the code WAKE, including an initial electron speed distribution centered on these values, have been performed. These showed no dependence of the results on this parameter.

Finally Thomson side-scattering has been included in the cylindrical version of the code by explicit calculation of the integral<sup>13</sup>

$$I_{\text{Th}}(y,z) \propto \int_{-\infty}^{+\infty} dt \int_0^{+\infty} dr \frac{n_e(r,z,t)I(r,z,t)}{\gamma^2(r,z,t)} \frac{r}{\sqrt{r^2-y^2}},$$

where  $(r,z)$  are the cylindrical coordinates,  $t$  is the time and  $y$  is the transverse coordinate in the plane of the scattered light image. According to the experimental features<sup>10</sup> a finite spatial resolution of  $15 \mu\text{m}$  is taken into account when performing the above integral. In the experiment the scattered light to an angle of  $90^\circ$  from the optical axis is spectrally filtered by a narrow-band filter centered over  $\lambda = 1.06 \mu\text{m}$  and collected by a lens. The side scattered intensity is assumed to behave as in incoherent relativistic Thomson scattering, that is to be proportional to the product  $n_e I/\gamma^2$ . This can be shown to be true for the incoherent Thomson scattering,<sup>27</sup> while the total scattered power in the case of coherent scattering is proportional to  $n_e^2$ .<sup>28</sup> The condition for the scattering to be incoherent is  $k\lambda_D \gg 1$ , where  $k$  is the wave number of the pulse and  $\lambda_D$  is the Debye length of the plasma. Temperatures of the order of some 10 eV can be expected due to the ionization mechanism, to the duration of the pulse and to the low density of the medium.<sup>26,29</sup> This gives a  $k\lambda_D$  product of the order of  $10^{-1}$  for the electronic densities used in this experiment. Thus, the Thomson side-scattering is coherent. However, the linear dependence on the electronic density can be shown to still apply to the spectrally unshifted component of Thomson side-scattering, which is detected through the narrow-band filter.<sup>30</sup> Moreover, Monot *et al.*<sup>10</sup> state that the linear relation between electron density and scattered intensity has been tested experimentally. A remark must be made concerning the Thomson scattering level compared to bremsstrahlung radiation. In the conditions of the following results it has been shown<sup>14</sup> that the Thomson signal exceeds the background noise by a factor of 10 and as a consequence is detectable.

We must point out that this particular measure, giving information on the product  $n_e I$ , is not the most suitable diagnostic for self-focusing. In fact, a general side effect of self-concentration of radiation is plasma density depletion.<sup>5,8</sup> The signal can, in principle, remain constant, while a strong self-focusing is produced causing the local plasma density to reduce. The best way to interpret this experiment is then to compare its results to simulations.

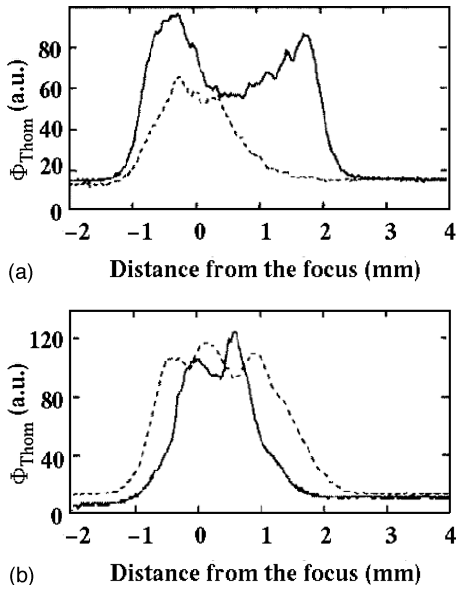


FIG. 1. Thomson scattering in a self-focusing experiment. Results by P. Monot *et al.* (Ref. 10). Experimental conditions: (a)  $n_e = 2.5 \times 10^{18} \text{ cm}^{-3}$  from a hydrogen jet,  $I = 2.8 \times 10^{17} \text{ W/cm}^2$  for the dashed curve and  $I = 2.8 \times 10^{18} \text{ W/cm}^2$  for the solid line curve; (b)  $n_e = 8 \times 10^{18} \text{ cm}^{-3}$  for the dashed curve and  $n_e = 10^{19} \text{ cm}^{-3}$  for the solid line curve,  $I = 2.8 \times 10^{18} \text{ W/cm}^2$ . Laser wavelength:  $\lambda = 1.06 \mu\text{m}$ ; pulse duration:  $T = 400 \text{ fs}$ ; waist radius:  $w_0 = 13 \mu\text{m}$ . The ratio to the critical power is, respectively,  $P/P_{\text{cr}} = 0.12, 1.2, 3.7,$  and  $4.7$ .

### III. SIMULATION RESULTS

In order to compare the measured quantities to our simulations, we reproduce the results of Monot *et al.*<sup>10</sup> in Fig. 1. The plotted curves correspond to an on-axis line scan of the Thomson side-scattering images. The two results in Fig. 1(a) are obtained with the same hydrogen density, corresponding to an electron density  $n_e = 2.5 \times 10^{18} \text{ cm}^{-3}$ . The incident peak intensity is  $I = 2.8 \times 10^{17} \text{ W/cm}^2$  for the dashed plot and  $I = 2.8 \times 10^{18} \text{ W/cm}^2$  for the solid line plot. Plot (b) shows two more results obtained with this peak intensity  $I = 2.8 \times 10^{17} \text{ W/cm}^2$  and with increased density, namely  $n_e = 8 \times 10^{18} \text{ cm}^{-3}$  for the dashed curve and  $n_e = 10^{19} \text{ cm}^{-3}$  for the solid one. The four cases correspond to increasing pulse to critical power ratios  $P/P_{\text{cr}} = 0.12, 1.2, 3.7,$  and  $4.7$ , respectively.

No self-guiding is expected in the first case, where the pulse power is far below the threshold. On the other hand, a further test is demanded for the remaining cases. In the general case of large values of the field amplitude  $a$ , self-guiding can occur for a given pulse power depending on the spatial variations of the phase of the pulse as it enters the plasma and on the ponderomotive modulation of the electron density. A simplified criterion for self-focusing within the paraxial approximation, taking into account the radial electron displacement (in the adiabatic approximation and in the absence of cavitation) has been introduced by Chen and Sudan.<sup>31</sup> A constant of propagation

$$H = \frac{1}{2\pi} \int \int \left[ |\nabla_{\perp} a|^2 - \left( \frac{\omega_p}{c} \right)^2 (\bar{\gamma} - 1)^2 - (\nabla_{\perp} \bar{\gamma})^2 \right] d^2 \mathbf{r}$$

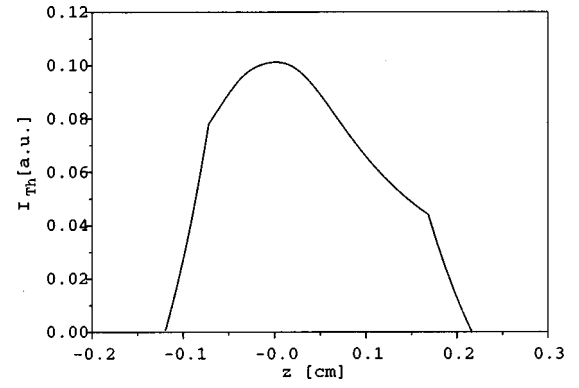


FIG. 2. Simulation of Thomson side-scattering from the optical axis. Conditions have been chosen to match the experimental parameters of the dashed curve in Fig. 1(a).

is found depending on the normalized complex amplitude of the vector potential

$$a = \sqrt{2} \frac{e\hat{A}}{mc^2},$$

and on the averaged Lorentz factor  $\bar{\gamma} = \sqrt{1 + |a|^2}$ . The condition  $H < 0$  is sufficient for relativistic ponderomotive self-guiding of the wave. The initial phase of the pulse enters the criterion through the complex amplitude  $a$ .

We take the initial complex wave amplitude to have the form of a Gaussian beam<sup>32</sup>

$$a = \frac{a_0}{1 + i\zeta} \exp\left(-\frac{\rho^2}{1 + i\zeta}\right),$$

where the radius  $\rho = r/w_0$  is normalized to the waist radius  $w_0$  and  $\zeta = z/z_0$  is the longitudinal position normalized to the Rayleigh length  $z_0 = \pi w_0^2/\lambda$ .

Taking into account all the parameters, including plasma density and focal position in the gas jet (according to the  $z = 0$  position in the experimental Thomson scattering plots), we obtain for the four cases, respectively,  $H = 0.055, 0.39, 0.014,$  and  $-0.12$ . So, in spite of the overcritical powers, the self-guiding of the pulse should be assured just in the last case, according to the condition  $H < 0$ .

The simulation reported in Fig. 2 corresponds to a power  $P = 0.12 P_{\text{cr}}$  and a constant  $H = 0.055$  and should be compared with the dashed curve of Fig. 1(a). One sees immediately that the maximum positions and the shapes of the two curves are similar. The full width half maximum (FWHM) width of the Thomson scattering plot is approximately equal to 0.14 cm in the experiment and to 0.20 cm in the simulation. A reason for this difference can be found in the experimental uncertainty of the focal position. This is determined directly at low power and eventually corrected by a high power shift. As a result, an uncertainty of about half a Rayleigh length ( $\Delta z = 250 \mu\text{m}$ ) must be taken into account for this position.<sup>33</sup> A simulation has been performed with the focus shifted by  $\Delta z$  towards the source (i.e., backwards in the plot variables). With this change the width of the curve falls to 0.16 cm, which is very close to the experimental value.

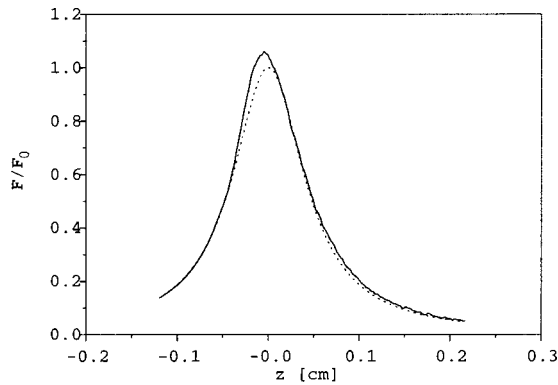


FIG. 3. Simulated fluence,  $F(0,z)$ . Same conditions as for Fig. 1(a), dashed curve. The dotted line corresponds to vacuum propagation.

No other features of the interaction seem affected by the focal position uncertainty in this case, so the simulation shown in Fig. 2 can be used to interpret the experiment. In Fig. 3 we can see the pulse fluence on axis  $F(r=0,z)$  as it has been computed by the simulation. This quantity corresponds to the time integral of the instantaneous intensity

$$F(r,z) = \int_{-\infty}^{+\infty} I(r,z,t) dt.$$

The fluence allows considerations of the concentration of energy around the optical axis: a perfectly guided short pulse, for instance, has the same fluence profile  $f(r) = F(r,z)$  at any  $z$ , while the radial distribution of the fluence of a diverging pulse has a mean radius growing with  $z$ . Moreover, the focus of a non-Gaussian pulse can be defined as the maximum of fluence. In Fig. 3 the on-axis fluence of the self-focused pulse (solid line) can be compared to the vacuum limit (dotted line). Both the curves are normalized to the maximum fluence in vacuum. The propagation of the pulse in this case is quasi-Gaussian with the focus being very close to the vacuum position  $z=0$ . The maximum fluence exceeds the vacuum limit by a factor of only 1.1. This implies that the relativistic focusing effect is small in this case.

In Fig. 4 we show the simulation corresponding to the second experimental result of Fig. 1(a), corresponding to  $P$

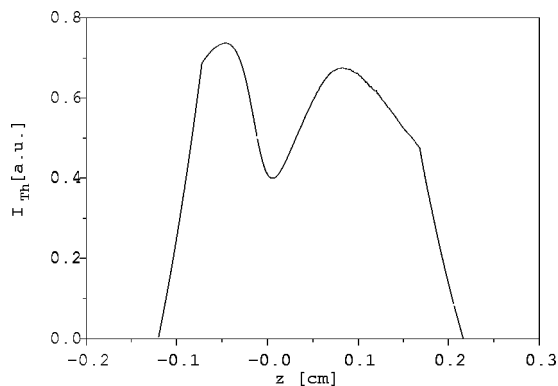


FIG. 4. Simulation of Thomson side-scattering from the optical axis. Condition have been chosen to match the experimental parameters of the solid line curve in Fig. 1(a).

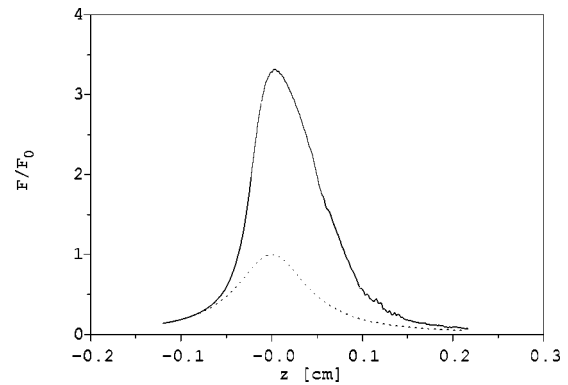


FIG. 5. Simulated fluence,  $F(0,z)$ . Same conditions as for Fig. 1(a), solid line curve. The dotted line corresponds to a vacuum propagation.

$= 1.2P_{cr}$  and a self-focusing parameter  $H = 0.39$ . In this case too, the simulation result is very similar to the experimental curve. We have to point out that the experimental curves in Fig. 1(a) have been normalized independently<sup>33</sup> (as one can check by working out the ratio of the data in the ascending part of the plots, where the interaction is still weak and the signal is substantially proportional to intensity), while our plots in Figs. 2 and 4 have consistent arbitrary units and show the right initial ratio.

As in the previous case, we show the fluence of the pulse in Fig. 5. The plot is similar to the previous one, with a converging part, a focus near the position  $z=0$  and a diverging part. A strong self-focusing occurs raising the maximum fluence by a factor 3.4. Nonetheless, in agreement with the  $H$  criterion, in spite of a pulse power  $P = 1.2P_{cr}$ , the pulse is not self-guided. It has to be remarked as well that the Thomson side-scattering signal has a minimum where the fluence (that is the average intensity) is maximum. Here the electron density must drop to minimize the product  $n_e I$ . We show in Fig. 6 both the laser intensity and the electron density  $n_e(r,t)$  distribution at the position  $z=0$  that is roughly the position of the maximum of fluence. As we can infer from the fluence plot, Fig. 6(a) shows that the laser pulse is focused to a maximum intensity that is more than three times the vacuum limit. At this position total cavitation of the plasma occurs, as shown in Fig. 6(b). After the end of the pulse electrons come back to the axis with a lower average density. This corresponds to the beginning of the formation of a channel, due to the radial momentum impressed by the pulse to the ions of the plasma.

We remark also that, due to the perfect cavitation, no radiation is scattered aside from the position  $(r=0, z=0)$  after the very beginning of the pulse.

In the same figure we can see another interesting feature. The borders of the plasma that are visible around the left corners of Fig. 6(b) correspond to the interface between the initially neutral  $H_2$  gas and the plasma. These borders are quite far from the high laser intensity regions, so ionization should not play an important role in the propagation of the main part of the pulse. This can be tested with our simulations by running the same calculations in a preformed plasma. As an example, the resulting laser intensity and electron density at focus for the same parameters of Fig. 4 are

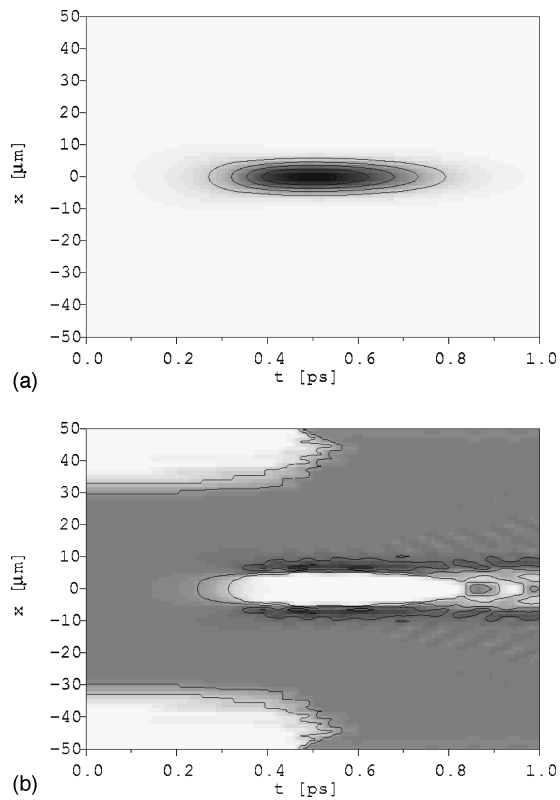


FIG. 6. Simulation of (a) laser pulse intensity and (b) electron density at nominal focus ( $z=0$ ). Same conditions as for Fig. 1(a), solid line curve. The pulse propagates from right to left. In (a) contours correspond to the intensities  $I=2, 4, 6,$  and  $8 \times 10^{18}$  W/cm<sup>2</sup>, respectively; in (b) to the densities  $n_e=1, 2, 3,$  and  $4 \times 10^{18}$  cm<sup>-3</sup>. Darker regions correspond to larger values.

shown in Fig. 7. The only visible differences between Figs. 6 and 7 occur on the density distribution plots where the gas-plasma boundary is absent in the preformed plasma case. On the other hand, the pulse shape and peak intensity are not affected by the ionization process. So one can state that, as far as the propagation of the pulse is concerned, the chosen experimental conditions allow a perfect decoupling of the effects of ionization from those of relativity and excitation of plasma waves. The Thomson scattering and fluence plots for the preformed plasma simulation also confirm that under these conditions propagation does not depend on the ionization process.

As a last remark we can look at pulse energy evolution during propagation. The normalized total energy of the laser pulse is plotted in Fig. 8. First, let us look at the dashed line which corresponds to the lower energy pulse. In this case, the total energy is constant within the numerical precision of the calculation until the end of the simulation, where the energy decreases due to the pulse diffracting out of the simulation box. On the other hand, the solid line, corresponding to the largest initial energy, is continuously decreasing for a total energy depletion of about 2% at the end of the gas jet (the final energy fall being here again an uninteresting geometrical effect). This amount of energy is given to plasma oscillations and to ion motion.

A signature of the interaction with plasma waves is the

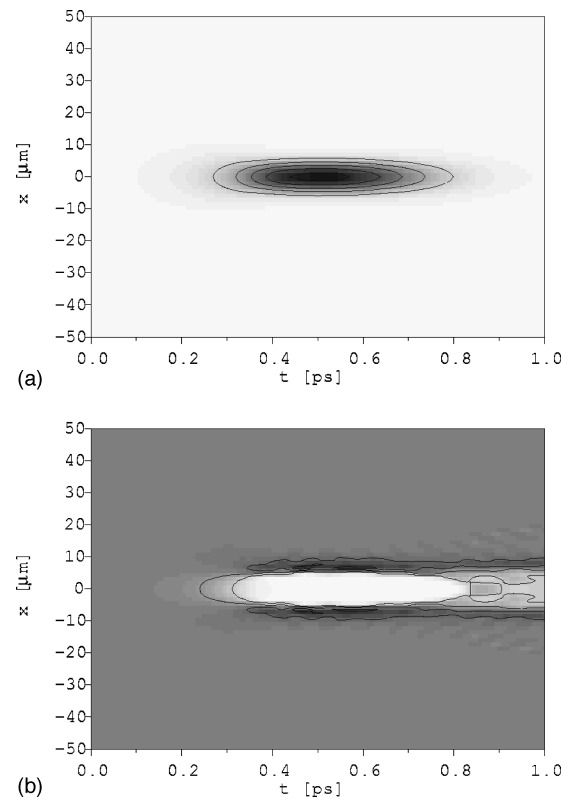


FIG. 7. Simulation of (a) laser pulse intensity and (b) electron density at nominal focus ( $z=0$ ) with no ionization interaction (preformed plasma). Same conditions as for Fig. 1(a), solid line curve. As in Fig. 6, the pulse propagates from right to left; the intensity contours correspond to  $I=2, 4, 6,$  and  $8 \times 10^{18}$  W/cm<sup>2</sup>, respectively; the densities contours to  $n_e=1, 2, 3,$  and  $4 \times 10^{18}$  cm<sup>-3</sup> and darker gray levels mean higher values.

pulse intensity modulation that is visible in Fig. 9(a) showing the pulse intensity distribution at the end of the flat top of the gas jet. This modulation has the typical frequency of plasma waves at the center of the gas jet,  $\omega_p$ . The corresponding electron wave has been pumped by the laser pulse and has taken part of its energy. In Fig. 9(b) the on-axis spectrum of the pulse, as measured by a typical spectrometer, is shown. We can see that the pulse has been spectrally shifted toward

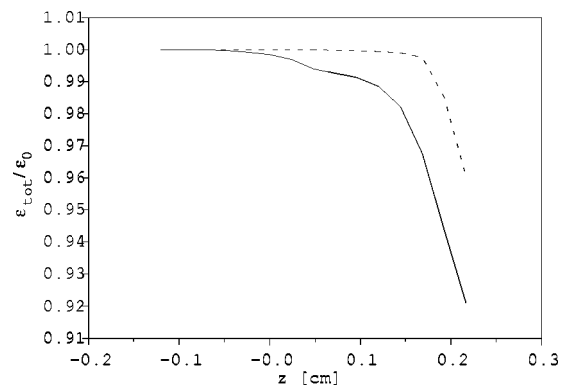


FIG. 8. Total pulse energy evolution. Simulation corresponding to the same conditions as Fig. 1(a). The strong depletion at the very end of the plots is due to the geometrical cut of the diverging pulse at the lateral borders of the simulation box. This does not correspond to an effective total electromagnetic energy depletion.

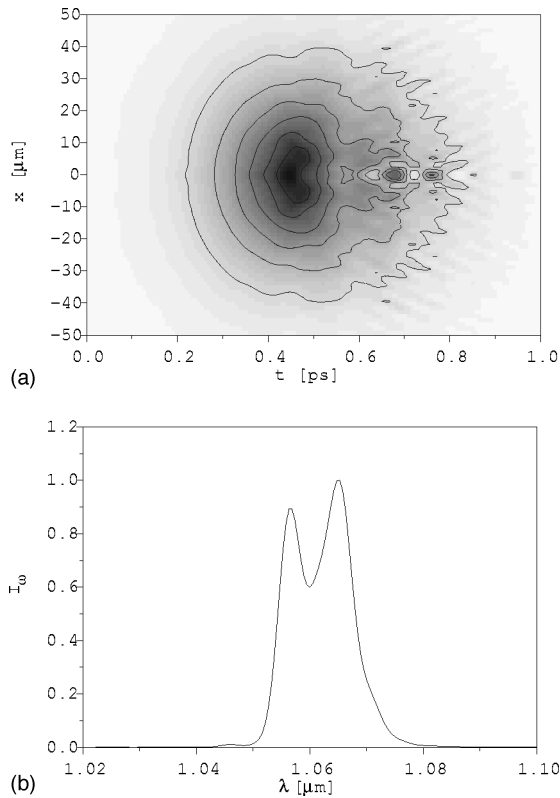


FIG. 9. Simulation of (a) intensity distribution at the end of gas jet ( $z=0.225$  cm) and (b) on-axis final spectrum. Same parameters as for Fig. 1(a). The contours in (a) correspond to the intensities  $I = 0.4, 0.8, 1.2, 1.6, 2.0,$  and  $2.4 \times 10^{17}$  W/cm<sup>2</sup>, respectively.

longer wavelengths. This “redshift” is due to the self-focusing phenomenon, increasing the refractive index temporally at the pulse position.<sup>34</sup>

When the electron density is raised up to  $n_e = 8 \times 10^{18}$  cm<sup>-3</sup> ( $P = 3.7P_{cr}$ ,  $H = 0.014$ ) and  $n_e = 10^{19}$  cm<sup>-3</sup> ( $P = 4.7P_{cr}$ ,  $H = -0.12$ ) corresponding to the experimental results of Fig. 1(b), the agreement between experimental and numerical results is reduced. In Fig. 10 we have reproduced the Thomson side-scattering signal for the conditions of Fig. 1(b). Dashed lines and solid lines must be compared, respectively. Some resemblances can still be pointed out between the dashed curves. Namely, both the dashed curve in Fig. 10

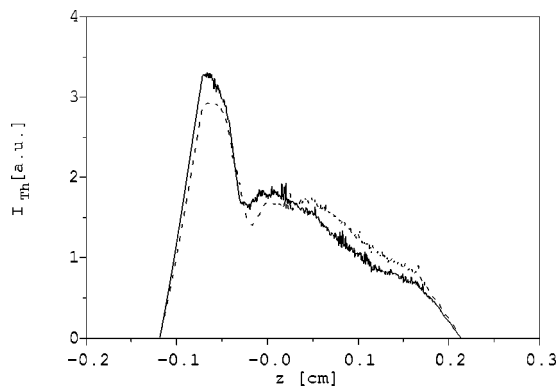


FIG. 10. Simulation of Thomson side-scattering from the optical axis. Same parameters as for Fig. 1(b).

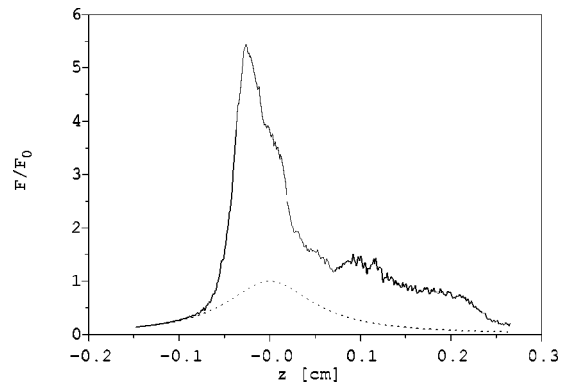


FIG. 11. Simulated fluence,  $F(0,z)$ . Same conditions as for Fig. 1(b), dashed line plot. The dotted line corresponds to a vacuum propagation.

and the one in Fig. 1(b) have a steep edge at about  $z = -0.1$  cm. They have comparable widths too. These features are lost in the comparison between the solid curves. The dramatic change of experimental Thomson scattering profile as the density is varied from  $n_e = 8 \times 10^{18}$  cm<sup>-3</sup> to  $n_e = 10^{19}$  cm<sup>-3</sup> is not reproduced by the simulation. Following Chiron *et al.*<sup>14</sup> the poor agreement between 2D cylindrical simulations and experimental results for the highest density can be attributed to filamentation and more generally to 3D effects. The analysis of the numerical results for the case where  $n = 8 \times 10^{18}$  cm<sup>-3</sup> can then give a qualitative picture of the interaction for the densities where filamentation occurs.

The on-axis simulated fluence for this electron density is shown in Fig. 11(a). The wave is first focused up to 5.5 times its fluence in vacuum and then defocused until the fluence reaches a value corresponding to the peak value in vacuum. After this point the fluence decreases slowly and self-guiding of the pulse occurs. This becomes even clearer by comparing the fluence plot to the energy evolution plot of Fig. 12. The total energy steadily decreases during the pulse’s propagation. Thus, the slow decrease in fluence is accompanied by a comparable decrease in energy, implying self-guided propagation.

At the fluence peak, complete electron cavitation occurs and ion motion starts before the end of the pulse, giving rise to plasma channeling. This is often accompanied by fast

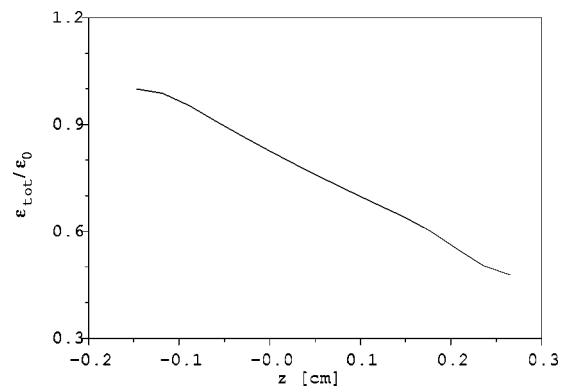


FIG. 12. Total pulse energy evolution. Simulation corresponding to the same conditions as Fig. 1(b), dashed line plot.

electron and strong magnetic field creation.<sup>8,22,17,35</sup> The simulation code also determines the fast electron spectrum and the low frequency magnetic field distribution. The calculated results should be accurate unless the electron longitudinal speed becomes higher than the group velocity of the laser pulse (which is not the case here). The fastest electrons are found for the highest electron density and correspond to energies up to 4 MeV. In the same simulation a maximum low frequency magnetic field of about 12MG has been found during the interaction. Values higher than these have been indicated in Refs. 17 and 35 with comparable intensities but with higher electron densities. In the very undercritical plasma limit, our simulations confirm the tendency of fast electron production to be associated with electron cavitation and channeling.

#### IV. CONCLUSION

In summary, our simulations closely match the experimental results as long as the total power is less or close to the critical power. A less accurate, but still satisfying, agreement is achieved up to about  $4P_{cr}$  where filamentation and 3D effects may come into play.

Concerning the interpretation of the experimental results, we can state, with other authors,<sup>10,14</sup> that near-critical laser pulses are not self-guided in the Monot experiment, while strong self-focusing and electron cavitation occur for  $P$  significantly larger than  $P_{cr}$ . Our simulations confirm previous numerical results and, by taking into account missing physics like transient effects, Raman instability and gas ionization validate them. While gas ionization effects happen to be negligible, pulse energy depletion due to Raman instability depends on pulse power and plasma density. For near-critical powers this depletion is very slow and pulse energy is effectively conserved until the end of the gas jet. The Raman instability energy depletion becomes important when the electron density is raised. In this case simulations using the adiabatic assumption for the electron response do not apply any more, while our simulation can still be used for data interpretation. A strong self-focusing occurs, followed by a self-guiding of the pulse, while the stimulated Raman scattering erodes the pulse. Finally, beam filamentation possibly occurs above about  $P=4P_{cr}$  preventing 2D numerical models from giving correct results.

#### ACKNOWLEDGMENTS

The authors thank P. Monot for providing them with detailed information about the experiment as indicated by Ref. 33. One of the authors (T.M.A.) is supported by the US Department of Energy and the National Science Foundation.

<sup>1</sup>G. Mourou and D. Umstadter, Phys. Fluids B **4**, 2315 (1992).

<sup>2</sup>E. Lefebvre and G. Bonnaud, Phys. Rev. Lett. **74**, 2002 (1995).

<sup>3</sup>S. Guérin, P. Mora, J. C. Adam, A. Héron, and G. Laval, Phys. Plasmas **3**, 2693 (1996).

<sup>4</sup>G. Schmidt and W. Horton, Comments Plasma Phys. Control. Fusion **9**, 85 (1985).

<sup>5</sup>G. Z. Sun, E. Ott, Y. C. Lee, and P. Guzdar, Phys. Fluids **30**, 526 (1987).

<sup>6</sup>P. Sprangle, E. Esarey, and A. Ting, Phys. Rev. A **41**, 4463 (1990).

<sup>7</sup>T. M. Antonsen, Jr. and P. Mora, Phys. Rev. Lett. **69**, 2204 (1992); Phys. Fluids B **5**, 1440 (1993).

<sup>8</sup>P. Mora and T. M. Antonsen, Jr., Phys. Rev. E **53**, R2068 (1996); Phys. Plasmas **4**, 217 (1997).

<sup>9</sup>A. B. Borisov, X. Shi, V. B. Karpov, V. V. Korobin, J. C. Solem, O. B. Shiryayev, A. McPherson, K. Boyer, and C. K. Rhodes, J. Opt. Soc. Am. B **11**, 1941 (1994).

<sup>10</sup>P. Monot, T. Auguste, P. Gibbon, F. Jackober, G. Mainfray, A. Dulieu, M. Louis-Jacquet, G. Malka, and J. L. Miquel, Phys. Rev. Lett. **74**, 2953 (1995).

<sup>11</sup>R. Wagner, S.-Y. Chen, A. Maksimonchuk, and D. Unstadter, Phys. Rev. Lett. **78**, 3125 (1997).

<sup>12</sup>K. Krushelnick, S. Ting, C. I. Moore, H. R. Burris, E. Esarey, P. Sprangle, and M. Baine, Phys. Rev. Lett. **78**, 4047 (1997).

<sup>13</sup>P. Gibbon, P. Monot, T. Auguste, and G. Mainfray, Phys. Plasmas **2**, 1305 (1995).

<sup>14</sup>A. Chiron, G. Bonnaud, A. Dulieu, J. L. Miquel, G. Malka, M. Louis-Jacquet, and G. Mainfray, Phys. Plasmas **3**, 1373 (1996).

<sup>15</sup>J. R. Marquès, F. Dorchie, P. Audebert, J. P. Geindre, F. Amiranoff, J. C. Gauthier, G. Hammoniaux, A. Antonetti, P. Chessa, P. Mora, and T. M. Antonsen, Jr., Phys. Rev. Lett. **78**, 3463 (1997).

<sup>16</sup>C. Stenz, F. Blasco, J. C. Pellicer, A. Antonetti, J. P. Chambaret, G. Chériaux, G. Darpentigny, G. Grillon, C. Le Blanc, A. Mysyrowicz, A. Rousse, and F. Salin, in *Ultrafast Phenomena X*, 10th International Conference on "Ultrafast Phenomena," San Diego, USA, 1996, edited by P. F. Barbara, J. G. Fujimoto, W. H. Knox, and W. Zinth (Springer Series in Chemical Physics Vol. 62, Berlin, Germany, 1996), p. 115; C. Stenz, F. Blasco, J. Stevefelt, J. C. Pellicer, A. Rousse, G. Chériaux, G. Darpentigny, G. Grillon, A. Mysyrowicz, A. Antonetti, and F. Amiranoff, in *X-ray Lasers 1996*, 5th International Conference on "X-ray lasers," Lund, Sweden, 1996, edited by S. Svanberg, and C. G. Wahlstrom (Institute of Physics Conference Series Vol. 151, Bristol, UK, 1996), p. 296.

<sup>17</sup>M. Borghesi, A. J. McKinnon, L. Barringer, R. Gaillard, L. Gizzi, C. Meyer, O. Willi, A. Pulkhov, and J. Meyer-ter-Vehn, Phys. Rev. Lett. **78**, 871 (1997).

<sup>18</sup>P. Sprangle, E. Esarey, J. Krall, and G. Joyce, Phys. Rev. Lett. **69**, 2200 (1992).

<sup>19</sup>N. E. Andreev, L. M. Gorbunov, V. I. Kirsanov, A. A. Pogossova, and R. R. Ramazashvili, JETP Lett. **55**, 571 (1992).

<sup>20</sup>C. D. Decker, W. B. Mori, and T. Katsouleas, Phys. Rev. E **50**, R3338 (1994); K.-C. Tzeng, W. B. Mori, and C. D. Decker, Phys. Rev. Lett. **76**, 3332 (1996).

<sup>21</sup>S. V. Bulanov, I. N. Inovenko, V. I. Kirsanov, N. M. Naumova, and A. S. Sakharov, Phys. Fluids B **4**, 1935 (1992).

<sup>22</sup>L. Gorbunov, P. Mora, and T. M. Antonsen, Jr., Phys. Rev. Lett. **76**, 2495 (1996).

<sup>23</sup>P. Chessa, Ph.D. thesis, Université de Paris VI, Paris, France, 1996.

<sup>24</sup>A. M. Perelomov, V. S. Popov, and M. V. Terent'ev, Sov. Phys. JETP **23**, 924 (1965).

<sup>25</sup>M. V. Ammosov, N. B. Delone, and V. P. Krainov, Sov. Phys. JETP **64**, 1191 (1986).

<sup>26</sup>D. Bauer, Phys. Rev. A **55**, 2180 (1997).

<sup>27</sup>I. H. Hutchinson, *Principles of Plasma Diagnostics* (Cambridge University Press, Cambridge, 1990), p. 239.

<sup>28</sup>H. A. Baldis, D. M. Villeneuve, and C. J. Walsh, Can. J. Phys. **64**, 961 (1986).

<sup>29</sup>S. C. Rae, Ph.D. thesis, Oxford University, UK, 1991.

<sup>30</sup>F. Jackober, Ph.D. thesis, Université de Paris XI, Orsay, France, 1996.

<sup>31</sup>X. L. Chen and R. N. Sudan, Phys. Rev. Lett. **70**, 2082 (1993).

<sup>32</sup>M. V. Klein and T. E. Furtak, *Optics* (Wiley, New York, 1986), p. 468.

<sup>33</sup>P. Monot (private communication, 1998).

<sup>34</sup>A. Bendib, A. Tahraoui, K. Kalache, P. Chessa, and P. Mora, Opt. Commun. **142**, 146 (1997).

<sup>35</sup>J. Fuchs, G. Malka, J. C. Adam, F. Amiranoff, S. D. Baton, N. Blanchot, A. Heron, G. Laval, J. L. Miquel, P. Mora, H. Pepin, and C. Rousseaux, Phys. Rev. Lett. **80**, 1658 (1998).